Research Article　|　🔓 **Full Access**

Efficient and Stable $Gd_3Ga_5O_{12}$:Cr^{3+} Phosphors for High-Performance NIR LEDs

Chen Jin, Ruiyang Li, Yongfu Liu ✉, Liangliang Zhang, Jiahua Zhang, Peng Sun, Zhaohua Luo, Jun Jiang ✉

Abstract

Cr^{3+}-activated $Gd_3Ga_5O_{12}$ garnet (GGG:Cr^{3+}) near-infrared (NIR) phosphors have shown promising applications in regulating plant growth. However, the low external quantum efficiency (EQE) results in a wall-plug efficiency (WPE) of phosphor-converted light-emitting diodes (pc)-LEDs of only ≈15%. Herein, an easy strategy to improve the luminescent properties of the GGG:Cr^{3+} phosphor is reported. Through optimization of the synthesized technology, the EQE is enhanced to 43.6%. Remarkably, the fabricated pc-LEDs achieve a WPE as high as 34.3%. These results demonstrate a significant advancement in the development and applications of NIR phosphor materials and NIR pc-LED devices.

1 Introduction

Near-infrared (NIR) light sources have a wide range of applications, including food quality testing and analysis, night vision, bio-tissue imaging, and plant growth regulators.[1-10] NIR phosphor-converted light-emitting diodes (NIR pc-LEDs) are the next-generation NIR light sources, constructed by using commercial blue LED chips and NIR-emitting phosphors.[11] The tiny size of blue chips and the broadband and tunable NIR spectrum of NIR phosphors make NIR pc-LEDs suitable for smart devices. Thus, NIR phosphors that can be pumped by blue LED chips and emit a wideband spectrum are emerging and attracting immense attention globally.[12-19]

Currently, many types of NIR phosphors have been reported, and most of them are based on inorganic matrixes doped by activators such as Cr^{3+}.[17-23] The electron structure of Cr^{3+}

$3d^3$ is strongly dependent on the crystal-field strength from the matrixes, resulting in tunable NIR spectra.[11, 19] For instance, Cr^{3+}-activated NIR phosphors employed borates,[20, 21] phosphates,[22] and fluorides[23] to demonstrate broadband emission in the spectral range of 650–1400 nm. The quantum efficiency and thermal stability of NIR phosphors are critical factors in determining the performance of NIR pc-LEDs. Thus, greater efforts have been devoted to achieving high efficiency and high thermal stability in NIR phosphors.

Garnet-based NIR phosphors typically exhibit high efficiency and good thermal stability.[24-32] To achieve high performance in NIR pc-LEDs, researchers have investigated the pursuit of high luminescent properties in materials by optimizing the preparation technology and composition design. For instance, Huber et al. reported the luminescence of Cr^{3+} in the $Gd_3Ga_5O_{12}$ garnet (GGG:Cr^{3+}) in 1983.[33, 34] Marciniak et al. introduced GGG:Cr^{3+} into thermometry in 2018.[35] In 2014, Zabiliūtė et al.[36] synthesized the GGG:Cr^{3+} phosphor by the sol-gel method and regarded it as the most promising material for photomorphogenesis LEDs due to its suitable luminescence spectra (excitation at 450 nm and emission at 700–760 nm). However, the reported internal quantum efficiency (IQE) pumped by blue light was only 30% due to impurities and defects in the lattice.[36] Lei et al. synthesized the GGG:Cr^{3+} phosphor using a solid-state method and improved the IQE to 90.3% by the substitution of Lu and Al for Gd and Ga, respectively.[37] The substitution slightly shifted the luminescence spectra to the blue region and achieved a good external quantum efficiency (EQE, 32%) and thermal stability (75% at 150 °C).[37] The fabricated NIR pc-LED effectively regulated photomorphogenesis of plants, as demonstrated by Lei et al.[37] and Li et al.[38, 39] However, the wall-plug efficiency (WPE) of reported NIR pc-LEDs was only ≈15% at the initial state.[37, 39]

In this study, we synthesize the GGG:Cr^{3+} phosphor by adding H_3BO_3 as a fluxing agent in the solid-state method. By optimizing the concentrations of H_3BO_3 and Cr^{3+}, the EQE is improved to 43.6%, and the emission intensity at 150 °C can keep 92.7% of that at room temperature (RT). The WPE reaches as high as 34.3%, which is almost the best value reported so far. These results demonstrate that this study provides an easy and effective strategy to develop excellent NIR phosphors and will greatly advance the development and applications of NIR pc-LEDs devices.

2 Results and Discussion

Powder samples were designed based on the nominal composition of $Gd_3Ga_{5-x}O_{12}$:xCr^{3+} (GGG:xCr^{3+}, x = 1–16%). Since the ionic radius of Ga^{3+} (0.062 nm) is close to that of Cr^{3+} (0.0615 nm), Cr^{3+} was designed to substitute Ga^{3+}.[37-40] To reveal the intrinsic characteristics of GGG:Cr^{3+}, the powder sample with a single garnet phase was achieved by the coprecipitation method.[32] As **Figure 1a** depicts, the Rietveld refinement results (R_{wp} = 5.77%, R_p = 4.48%, and χ^2 = 1.22) for the X-ray diffraction (XRD) pattern of GGG:2.5% Cr^{3+} confirmed that the sample crystallizes into the single garnet phase. The detailed atomic

coordinates, site occupancy, cell parameters, and bond lengths for the GGG:2.5% Cr^{3+} sample were listed in Tables S1–S3 (Supporting Information). The garnet structure was shown in Figure 1b. Gd^{3+} is located at the center of the [GdO_8] dodecahedron, while Ga^{3+} has two sites coordinated with four and six O^{2-} anions, forming the [GaO_4] tetrahedra and [GaO_6] octahedra, respectively. These observations confirm that Cr^{3+} replaces Ga^{3+} sites. The Raman spectrum in Figure 1c shows some vibrational peaks in the frequency band of 100–300 cm^{-1} for the [GdO_8] dodecahedra. The vibration frequency ranges of 300–450 and 650–850 cm^{-1} are from the [GaO_6] octahedra and the [GaO_4] tetrahedra, respectively.[25, 37-39] The garnet crystal structure can be directly observed at an atomic-scale resolution using the high-angle annular dark-field (HAADF) scanning transmission electron microscopy (STEM) tomography. GGG displays a typical cubic structure projected along the [001] direction (Figure 1d), and the peaks on the line scan curve correspond to the Gd and Ga atomic arrays in the HAADF-STEM image (Figure 1e). From the ordered Ga distribution, the octahedron position is exclusively occupied only by Ga.
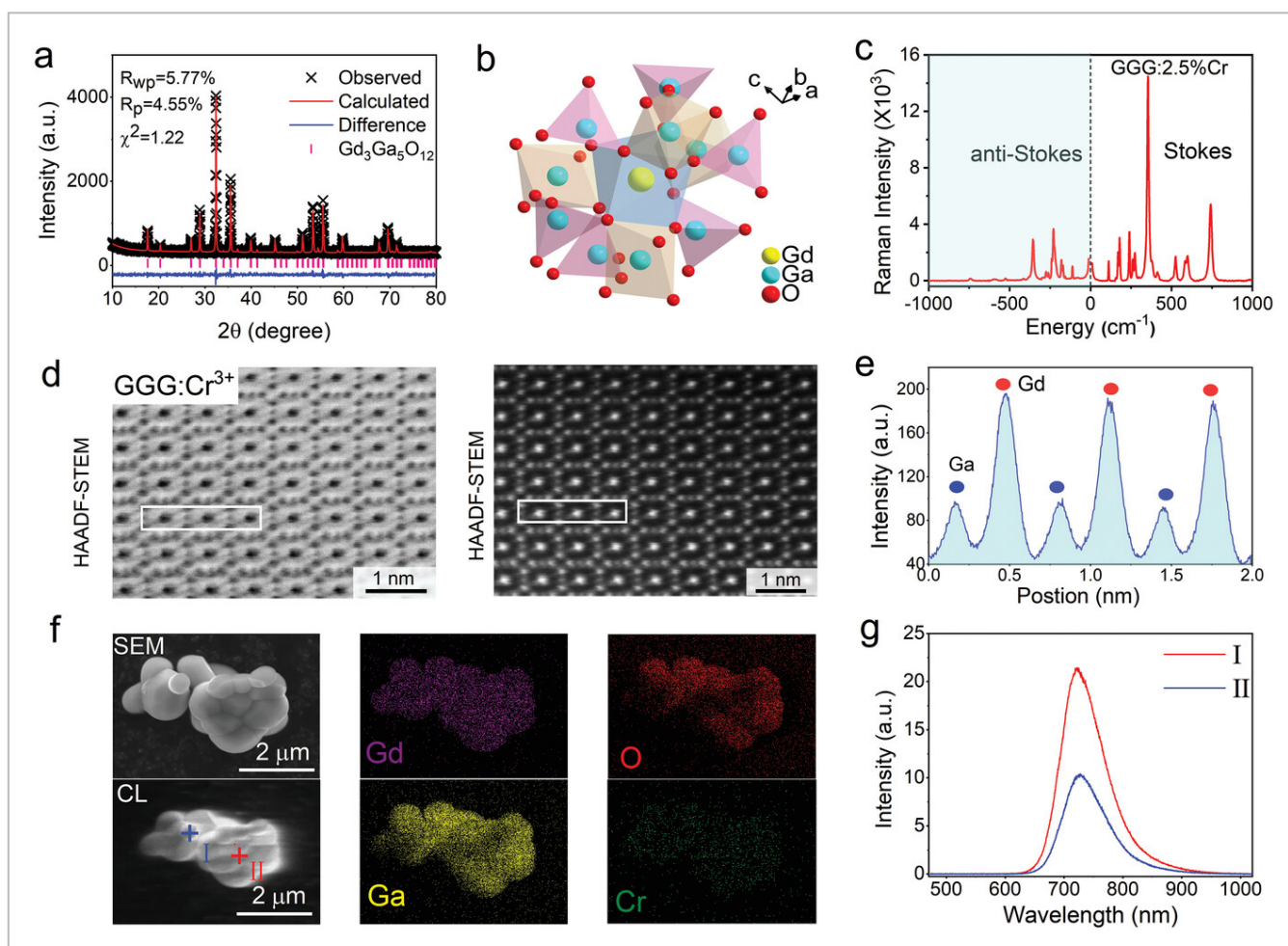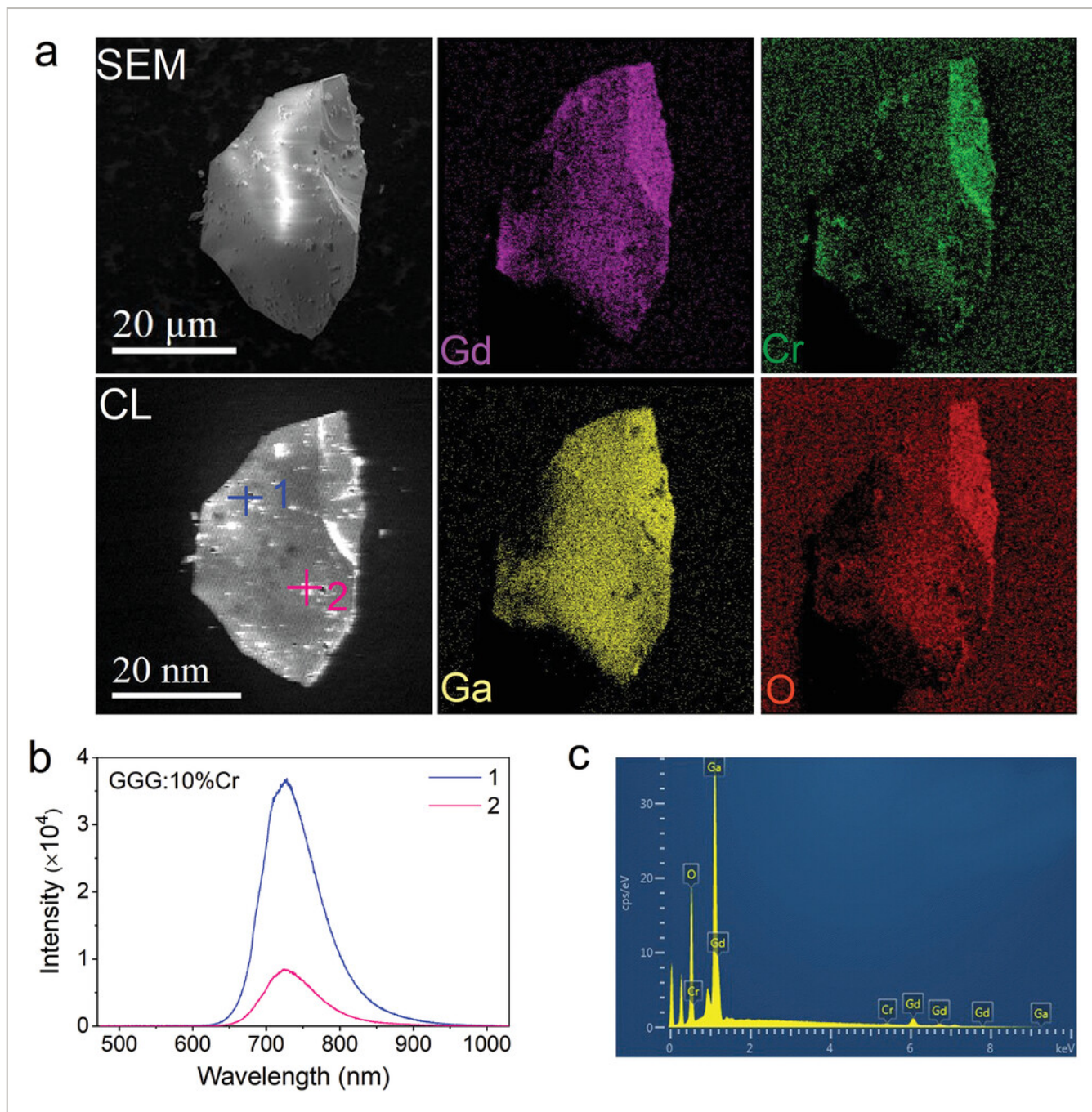

Figure 1

Open in figure viewer | ⬇PowerPoint

a) Rietveld refinements for XRD pattern, b) coordination environments of Ga^{3+} and Gd^{3+}, c) Raman spectrum, HAADF-STEM images d) and line scans of Gd and Ga columns e), SEM, CL, and EDS elemental mapping images f) and CL spectra

at points I and II g). All measurements are from GGG:2.5%Cr^{3+} fabricated by a coprecipitation method.

Figure 1f shows the scanning electron microscopy (SEM) image and the energy dispersive X-ray spectroscopy (EDS) element mapping image of GGG:2.5%Cr^{3+}. The images show that the powder particles have dimensions of ≈2–5 μm, and the elemental distribution of Ga, Gd, O, and Cr is almost homogeneous, with measured elemental ratios close to theoretical values (Figure S1 and Table S4, Supporting Information). The cathodoluminescence (CL) image based on the SEM reveals the Cr^{3+} luminescence in the GGG host, with NIR luminescence peaking at 725 nm in the CL spectra of GGG:Cr^{3+} in Figure 1g, which is consistent with the reported results.[34] These findings demonstrate the successful doping of Cr^{3+} into the GGG host. However, the CL intensity is inhomogeneous, with the bright area (point I) being more than twice as strong as the dark area (point II).

The coprecipitation method synthesized powder sample exhibits feeble luminescence, similar to the luminescence of GGG:Cr^{3+} as reported by the sol-gel method.[36] This could be attributed to the small particle size. It is a common phenomenon that luminescence weakens as the particle size of phosphors decreases, owing to the defects on the particle surface. The SEM image in Figure 1f displays a powder size of ≈200–500 nm. Thus, to improve the luminescence, the powder samples are optimized and synthesized via a solid-state method. The SEM, CL spectra, and EDS element mapping images of GGG:10%Cr^{3+} are shown in **Figure** 2. The SEM images reveal that the size of the powder prepared by the high-temperature solid-phase method is ≈10–30 μm. The increased grain size of the powder can enhance luminous efficiency. However, the CL spectra demonstrate that the luminescence is not uniform and the intensities vary. The CL spectral intensity in the bright region (point 1) is over four times stronger than that in the dark region (point 2) (Figure 2b). The EDS images illustrate the uneven distribution of Ga, O, Gd, and Cr (Figure 2c). Taking Gd as the standard, the elemental ratios of Gd and Cr measured are proximate to the theoretical values, but the experimental values of Ga and O are significantly lower than the theoretical values. This may be due to the loss of Ga element caused by the partial volatilization of Ga$_2$O$_3$ in the high-temperature sintering process (Table S5, Supporting Information).

Figure 2
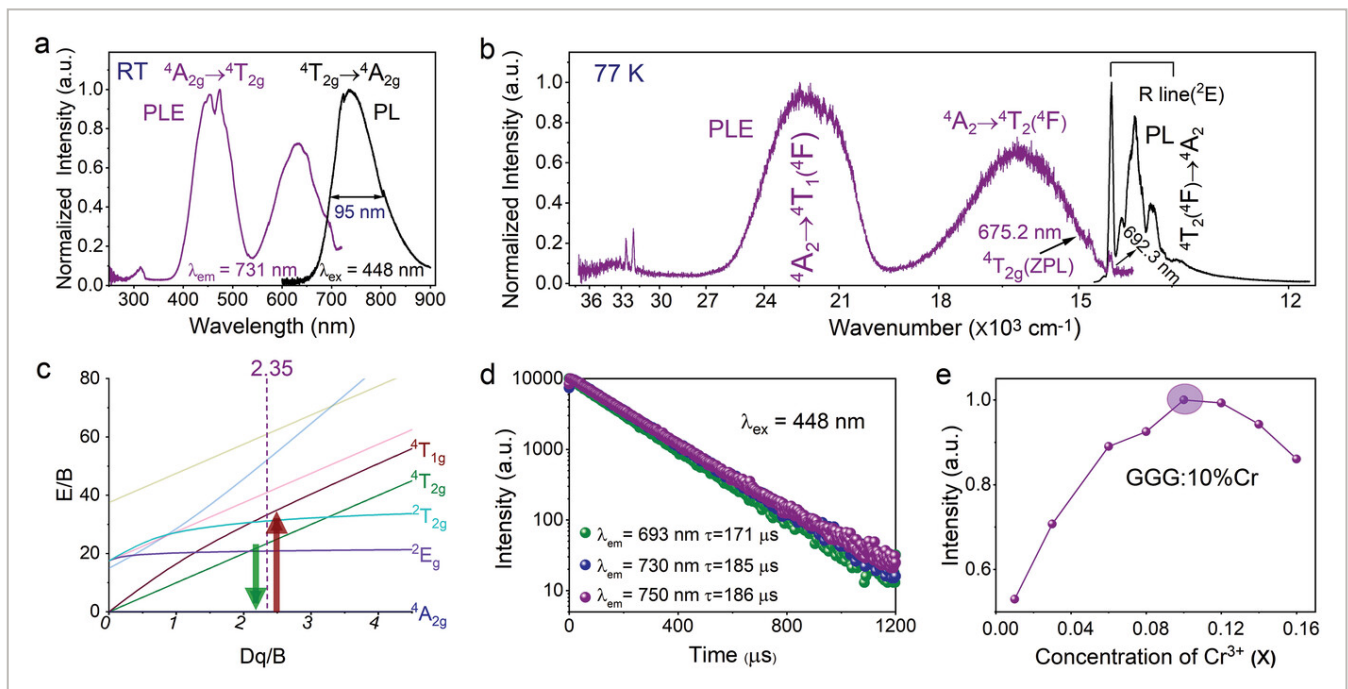
Open in figure viewer | ⬇PowerPoint

a) SEM, CL, and EDS elemental mapping images. b) CL spectra at points 1 and 2, and c) EDS spectra of GGG:10%Cr^{3+} fabricated by the high-temperature solid-state method.

The addition flux H_3BO_3 can greatly enhance the photoluminescence (PL) (Figure **S2a**, Supporting Information). The optimal amount of H_3BO_3 is 3 wt.%. The GGG:10%Cr^{3+} + 3 wt.% H_3BO_3 sample exhibits a maximum PL intensity, which is >50% higher to that of the H_3BO_3-free sample (Figure **S2b**, Supporting Information). The introduction of H_3BO_3 can reduce the sintering temperature, improve the crystallinity of the sample, and enhance the luminous intensity.[24, 37] However, in addition to the GGG phase, a few $GdBO_3$ impurities are observed

in the XRD patterns of the GGG:xCr^{3+} (x = 1–16%) samples with H_3BO_3 (Figure S3, Supporting Information). These results indicate that the addition of Cr^{3+} into the matrix lattice does not affect the garnet structure, but the introduction of H_3BO_3 produces the $GdBO_3$ heterophase. This may further indicate that the volatilization of Ga_2O_3 leads to the relative excess of Gd element, which provides conditions to form the $GdBO_3$ phase by the combination of B and Gd. However, the ionic radii of Gd^{3+} (1.053 nm) and B^{3+} (0.082 nm) are quite different from Cr^{3+} (0.0615 nm), and there is no suitable lattice for Cr^{3+} luminescence in the $GdBO_3$ lattice. Therefore, the effect of $GdBO_3$ on the luminescent peak pattern of GGG:Cr^{3+} could be expected to be negligible. To simplify the description, the optimized sample GGG:10%Cr^{3+} + 3 wt.% H_3BO_3 is referred to as GGG:10%Cr^{3+}.

The GGG:Cr^{3+} samples were sintered in an ambient air atmosphere. To diagnose the valence state of Cr, the diffuse reflection (DR) spectrum was measured. The DR spectrum of GGG:10% Cr^{3+} is almost uniform between 1000 and 1600 nm proving the absence of Cr^{4+} absorption (Figure S4, Supporting Information). The absorption bands at 251, 448, and 616 nm are attributed to the Cr^{3+} transitions from $^4A_{2g}$ to $^4T_{1g}(4P)$, $^4T_{1g}(4F)$, and $^4T_{2g}(4F)$, respectively.[33, 34] The DR spectrum is consistent with the photoluminescence excitation (PLE) bands centered at 448 and 630 nm in **Figure 3a**. The weak PLE band ≈306 nm originates from the $^8S_{7/2} \rightarrow {}^6I_j$ transition of Gd^{3+}.

Figure 3

a) PL and PLE spectra recorded at RT and b) 77 K, c) Tanabe–Sugano energy diagram, and d) Fluorescent decay curves of GGG:10%Cr^{3+}. e) PL intensities of GGG:xCr^{3+} (x = 1–16%) with 3 wt.%H_3BO_3.

At RT, the PL spectrum of GGG:10%Cr^{3+} shows a broad band that peaks at 731 nm and has a full-width at half maximum (FWHM) of 95 nm. This broadband NIR emission is the same as the luminescence reported by Huber et al.,[34-38] which is caused by the spin-allowed transition of $^4T_{2g} \rightarrow {}^4A_{2g}$. At a low temperature, the PL spectrum transforms into sharp peaks at 693, 712, and 725 nm (Figure **3b**) due to the $^2E_g \rightarrow {}^4A_{2g}$ transitions.[34] The sharp peaks detected in both the PLE and PL spectra at the same wavelength region corresponding to the zero-phonon line (ZPL) of the ^2E_g (R-lines) energy level, which is located at 692.3 nm (14 445 cm^{-1}) in the PLE spectrum. The tiny peaks observed at 675.2 nm (14 810 cm^{-1}) in the PLE spectrum are the ZPL of the $^4T_{2g}$ energy level. The energy gap between the ^2E_g R-line and the $^4T_{2g}$ ZPL is 366 cm^{-1}, which is close to the value of 380 cm^{-1} reported by Huber et al. in GGG:Cr^{3+}.[34] These results indicate a strong spin-orbit coupling (SOC) effect between the ^2E_g and $^4T_{2g}$ states, and then thermalization of these two states is allowed. Consequently, the emitting $^4T_{2g}$ and ^2E_g states are mixed by the SOC and electron-phonon coupling (EPC) effects.[34]

The corresponding crystal field parameters (Table **S6**, Supporting Information) can be calculated by using the Equation **3-2** developed by Tanabe and Sugano.[34, 41, 42]

$$ \tag{1} $$

$$ \tag{2} $$

$$ \tag{3} $$

Here, *Dq* and *B* represent the crystal field parameters of Cr^{3+}, with *B* being the Racah electron repulsion parameter. By choosing the energy at 77 K (wavenumber in Figure **3b**; Table **S6**, Supporting Information), *Dq* and *B* are calculated to be 1481 and 630 cm^{-1}. The *Dq/B* value indicating the crystal field strength is determined to be 2.35 and then the energy diagram of Cr^{3+} in the GGG matrix is illustrated in Figure **3c**. The ^2E_g emission is only identified at a low temperature (77 K). While at a high temperature, only the $^4T_{2g}$ emission is observed (PL@RT) due to the strong SOC and EPC effects. Therefore, at RT, all fluorescence decay curves monitored at 693, 730, and 750 nm show the single exponential model (Figure **3d**), giving a typical lifetime of 171–186 µs due to the spin-allowed $^4T_{2g}(4F) \rightarrow {}^4A_{2g}$ transition of Cr^{3+}.

The normalized PL spectra reveal that the spectral profiles of the GGG:Cr^{3+} samples are almost independent of the concentrations of Cr^{3+} (Figure **S5**, Supporting Information). The PL intensity reaches its maximum when the concentration of Cr^{3+} reaches 10% in Figure **3e**, and then the luminous intensity decreases gradually due to the concentration quenching effect.[24-28]

The thermal stability of the optimized GGG:10%Cr^{3+} sample is investigated. **Figure 4a** depicts the contour plots of the PL spectra of GGG:10%Cr^{3+} dependent on temperatures from RT to 573 K. Figure **4b** presents the normalized PL spectra of GGG:10%Cr^{3+} at different

temperatures. As the temperature increases, the PL peak positions gradually redshift. The peak position shifts from 740 to 783 nm when the temperature increases from RT to 573 K (Figure 4c). The redshift could be attributed to the weakened crystal-field strength caused by the lattice expansion when the sample is heated from RT to 573 K.[24, 25] Correspondingly, the EPC is strengthened, resulting in an extension of the FWHM from 95 to 147 nm (Figure 4c).[22, 27]
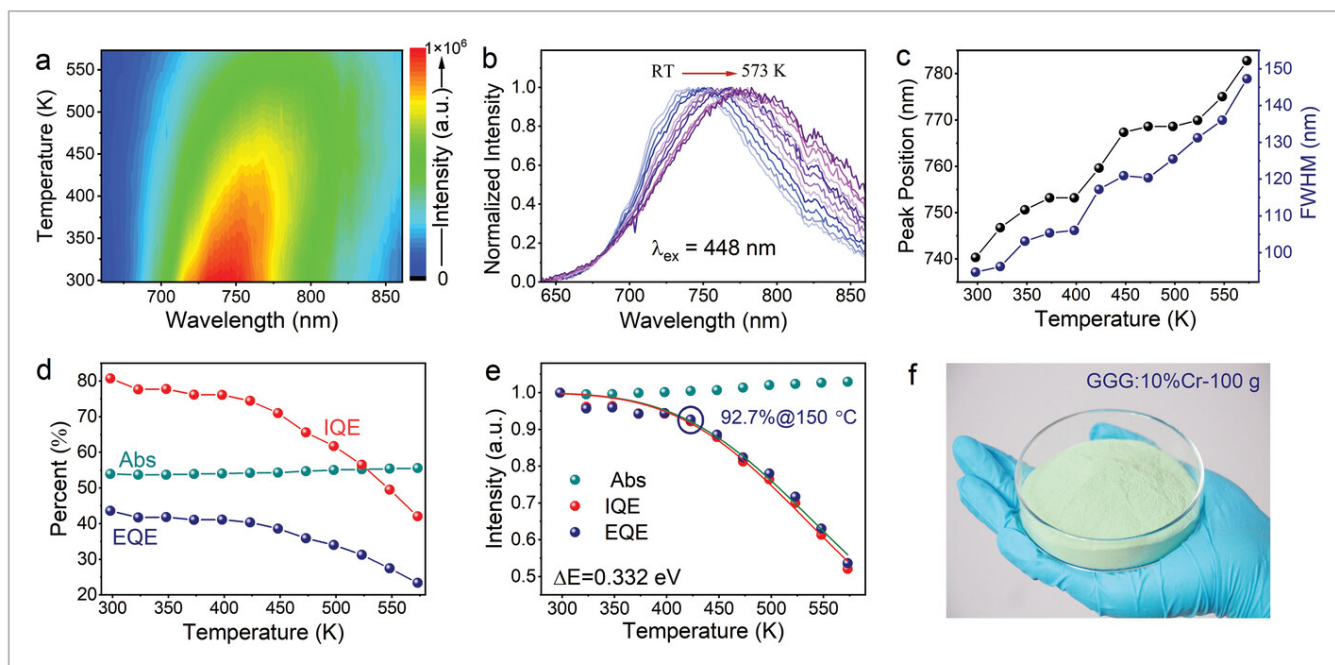
Figure 4

Open in figure viewer | ⬇PowerPoint

a) PL and b) normalized PL spectra, c) peak wavelength and FWHM, d) IQE, EQE, and Abs, and e) normalized IQE, EQE, and Abs of GGG: 10%Cr^{3+} dependent on temperatures from RT to 573 K. f) Photo of fabricated phosphors.

Figure 3d depicts the IQE, EQE, and absorbance (Abs) values of GGG:10%Cr^{3+} dependent on temperatures from RT to 573 K. The sample is pumped by the 448 nm blue light. At RT, the IQE and Abs are measured three times to assess their photoluminescence performances (Figure S6 and Table S7, Supporting Information), the average IQE and Abs were determined to be 80.8% and 54.0%, respectively. The EQE was determined to be 43.6% based on the relation of EQE = IQE *Abs.[24, 43] The errors of IQE and EQE were ≈1.2% and 0.6%, respectively. These results are listed in Table S8 (Supporting Information) as well. Notably, the EQE value of GGG:10%Cr^{3+} is exceptional compared to other reported NIR phosphors listed in Table S9 (Supporting Information). For instance, the EQE vales of $Gd_3Zn_{0.8}Ga_{3.4}Ge_{0.8}O_{12}:Cr^{3+}$,[39] $Gd_{2.4}Lu_{0.6}Ga_4AlO_{12}:Cr^{3+}$,[37] and $CaLu_2Mg_2Si_3O_{12}:Cr^{3+}$,[28] were 31.2%, 32%, and 38.6%,respectively. With the increase of temperature, the phosphor GGG:10% Cr^{3+} undergoes thermal quenching causing a gradual decrease in the luminescence intensity and IQE/EQE values. This phenomenon is caused by the strengthened thermal-activated non-radiative relaxation at high temperature, leading to a

decline in IQE.[24, 37] Because the Abs is slightly enhanced, thus the thermal quenching of EQE is slower than that of IQE (Figure **4e**). The activation energy of thermal quenching can be calculated using the Arrhenius Equation (**4**)[43-46]:

$$\tag{4}$$

where *I(T)* symbolizes the PL intensity at temperature T, *I(0)* means the PL intensity at 0 K, *c* denotes a constant, and *k* denotes Boltzmann's constant. The activation energy *ΔE* of GGG:10%Cr^{3+} is calculated to be 0.332 eV. The higher activation energy indicates that the probability of the thermal-activated non-radiative relaxation of the $^4T_{2g}$ state is challenging. [24, 26, 43, 44] Thus, GGG:10%Cr^{3+} shows good thermal stability. At 423 K the EQE maintains as high as 92.7% of the initial value at RT (Figure **4e**). This is significantly superior to that of most reported NIR phosphors (Table **S9**, Supporting Information). For example, at 423 K, EQE values were only 75%, 76%, 81.8%, and 88.4% in $Gd_{2.4}Lu_{0.6}Ga_4AlO_{12}:Cr^{3+}$,[37] $Ca_2LuScAl_2Si_2O_{12}:Cr^{3+}$,[31] $Gd_3Y_{0.5}In_{0.5}Ga_4O_{12}:Cr^{3+}$,[38] and $CaMg_{0.995}Al_{0.005}Si_{1.995}O_6:Cr^{3+}$,[44] respectively. In the amplification experiments, 100 g of GGG:10%Cr^{3+} powders were fabricated, and the sample exhibited a green body color (Figure **4f**), demonstrating the reproducibility of this phosphor (Figure **S7**).

Figure 5a displays the NIR pc-LED manufactured by using the reproduced GGG:10%Cr^{3+} phosphors and the commercial 448 nm blue LEDs (0.5 W). This low-power device illuminates ≈3 V and emits a milky white light in the pc-LED device, while exhibiting a bright red emission under the filter. Figure **5b** shows the emission peaks at ≈448 and 750 nm, originating from the blue chip and the GGG:Cr^{3+} phosphors, respectively. With rising working currents, the spectra intensity of the pc-LED device increases gradually. As can be seen from Figure **5c**, the rising driving current will lead to an increase of output power and a decrease of photoelectric efficiency. The output NIR power (from 600 to 1050 nm) rises from 9.2 to 119.1 mW when the driven current increases from 10 to 200 mA. Correspondingly, the wall-plug efficiency (WPE) from the input electric power to the output NIR light decreases from 34.3% to 17.9% (Table **S10**, Supporting Information). Benefiting from the high efficiency and outstanding thermal stability of the developed NIR phosphor, it is significant that the device shows the best performance reported so far (Table **S11**, Supporting Information).[47, 48] The contrast WPE values at 100 mA are further represented in Figure **5d**. The WPE reaches 24.5%, representing a record efficiency for NIR pc-LEDs reported so far.
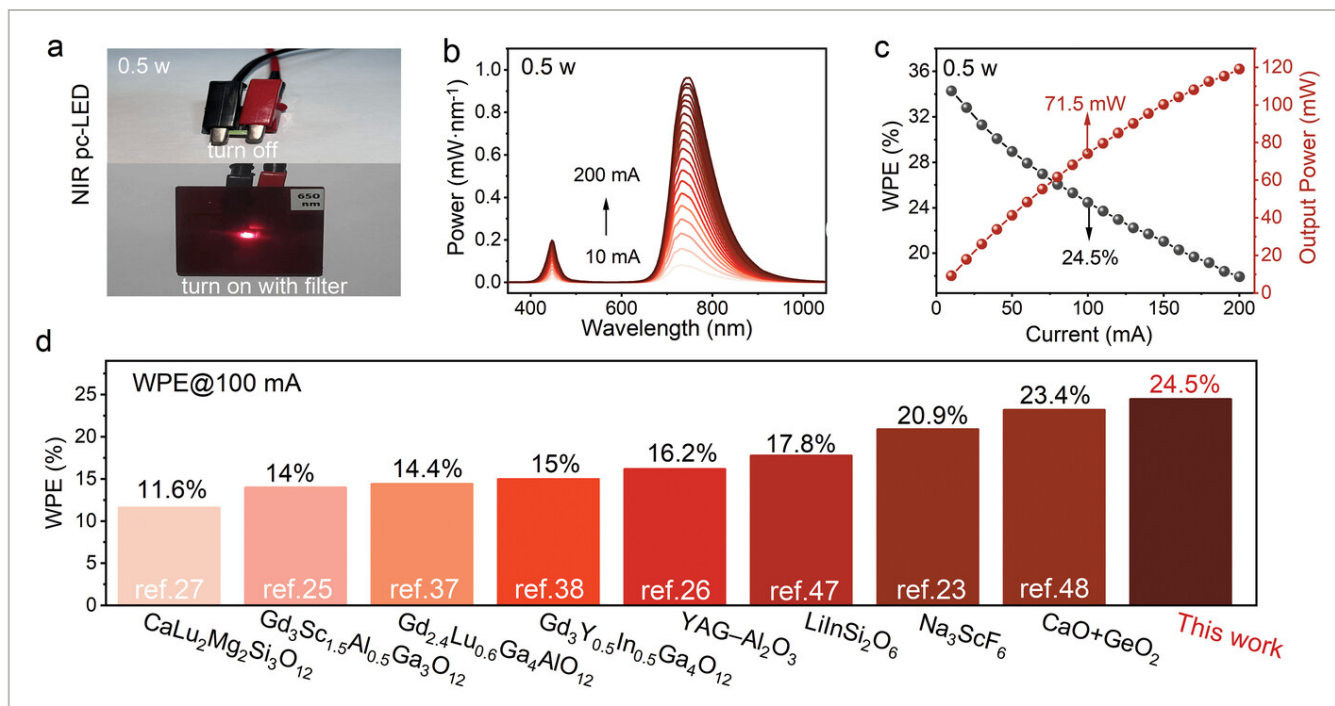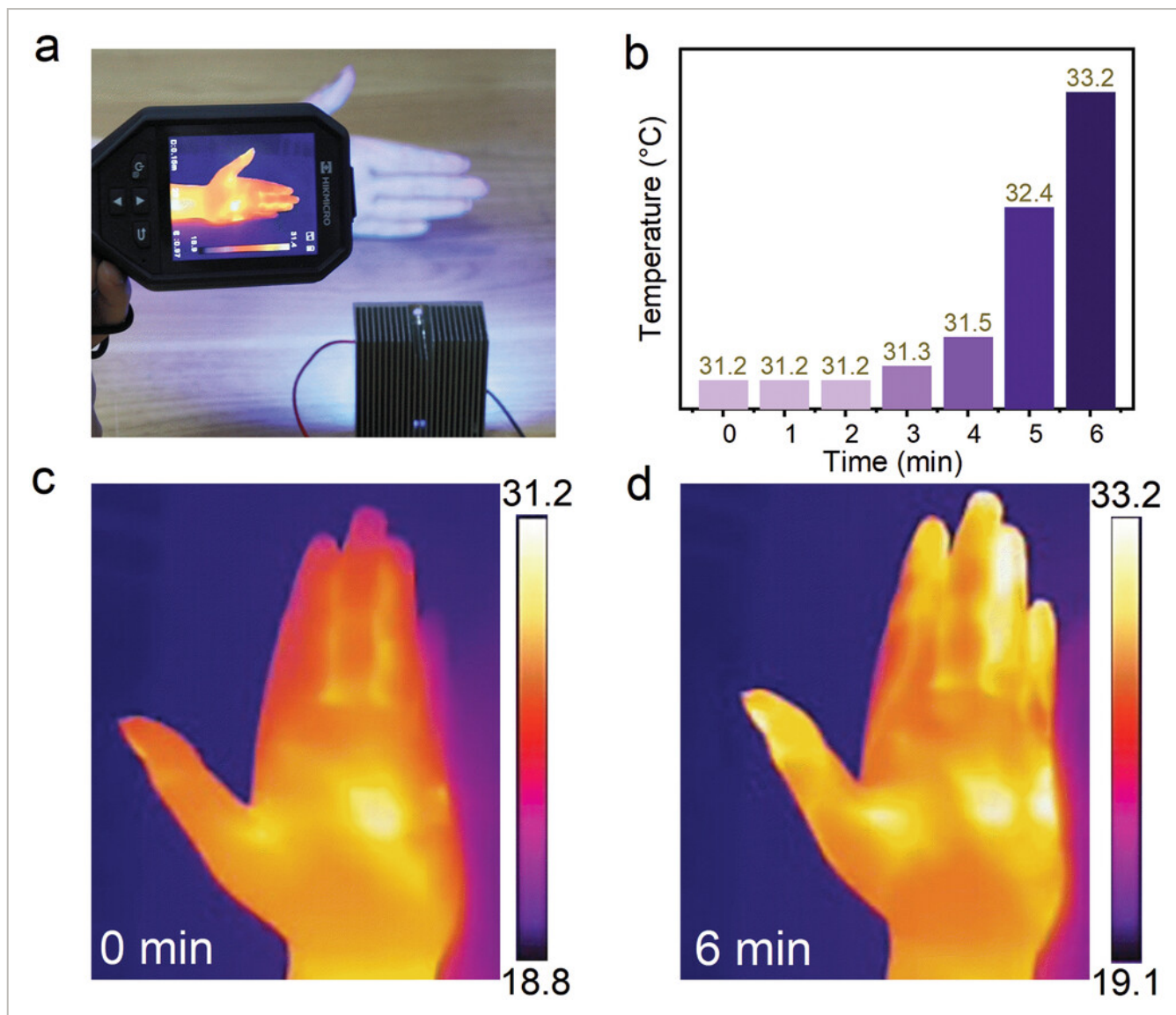
Figure 5

Open in figure viewer | ⬇ PowerPoint

a) Photographs, b) emission spectra, and c) output power of NIR light and photoelectric efficiency (WPE) of the fabricated NIR pc-LED (0.5 W) dependent on driving currents (10–200 mA). d) Progresses and comparations of WPEs for NIR pc-LEDs.

In addition to its applications of NIR light sources in night vision systems, food monitoring, plant growth, et al., we endeavor to extend the NIR pc-LEDs to the medical field.[49, 50] The hand of one of the authors was irradiated with NIR pc-LEDs, and the temperature of the hand was monitored and displayed in **Figure 6a**. As the human body is endothermy, the temperature of the palm remained at 31.2 °C for 3 min (Figure **6b**). After 6 min of illumination, the temperature gradually rises to 33.2 °C. These changes are also displayed in the thermal images of the palm taken at the initial 0 and 6 min, as shown in Figure **6c,d**. It is worth noting that the NIR pc-LED does not greatly heat the hand, and the temperature remains non-harmful. The NIR pc-LED illuminates intense NIR light ≈700–900 nm (Figure **5b**), which is beneficial to human skin. Thus, the NIR pc-LED holds great promise for applications in the health and medical fields.

Figure 6

Open in figure viewer | ⬇PowerPoint

a) Schematic image of temperature monitor of palm irradiated by NIR pc LEDs, b) Palm temperature dependent on irradiated times, and c,d) Infrared thermal images recorded at 0 and 6 min.

3 Conclusion

We developed an efficient NIR phosphor GGG:Cr^{3+} by a high-temperature solid-state reaction. By optimizing the sintering flux H$_3$BO$_3$ and Cr^{3+} concentrations, we have improved the EQE to 43.6%, which is superior to most NIR phosphors. Furthermore, the thermal stability of the phosphor keeps 92.7% at 423 K. The high efficiency and excellent thermal stability enabled us to realize the NIR pc-LED with an outstanding WPE of 34.3%, which is the highest reported result to date. It is believed that this study is a significant step forward in commercial applications of NIR phosphor materials and pc-LED devices.

Acknowledgements

Conflict of Interest

The authors declare no conflict of interest.

Open Research ⌄

Data Availability Statement

The data that support the findings of this study are available in the supplementary material of this article.

Supporting Information ⌄

Filename	Description
adom202300772-sup-0001-SuppMat.pdf 1.4 MB	Supporting Information

Please note: The publisher is not responsible for the content or functionality of any supporting information supplied by the authors. Any queries (other than missing content) should be directed to the corresponding author for the article.

References ⌄

1　Z. Lv, L. Jin, Y. Cao, H. Zhang, D. Xue, N. Yin, T. Zhang, Y. Wang, J. Liu, X. Liu, H. Zhang, *Light: Sci. Appl.* 2022, **11**, 116.

　　　　| **CAS** | **PubMed** | **Web of Science®** | **Google Scholar** |

2　H. Zhang, G. Wang, Z. Zhang, J. H. Lei, T.-M. Liu, G. Xing, C. X. Deng, Z. Tang, S. Qu, *Light: Sci. Appl.* 2022, **11**, 113.

CAS | **PubMed** | **Web of Science®** | **Google Scholar**

3　D. Li, Z. Hu, H. Zhang, Q. Yang, L. Zhu, Y. Liu, T. Yu, J. Zhu, J. Wu, J. He, P. Fei, W. Xi, J. Qian, D. Zhu, *eLight* 2022, **2**, 15.

Google Scholar

4　L. Lei, Y. Wang, A. Kuzmin, Y. Hua, J. Zhao, S. Xu, P. N. Prasad, *eLight* 2022, **2**, 17.

Google Scholar

5　M. D. Dramićanin, Ł. Marciniak, S. Kuzman, W. Piotrowski, Z. Ristić, J. Periša, I. Evans, J. Mitrić, V. Đorđević, N. Romčević, M. G. Brik, C. G. Ma, *Light: Sci. Appl.* 2022, **11**, 279.

CAS | **PubMed** | **Web of Science®** | **Google Scholar**

6　X. Chen, Y. Li, K. Huang, L. Huang, X. Tian, H. Dong, R. Kang, Y. Hu, J. Nie, J. Qiu, G. Han, *Adv. Mater.* 2021, **33**, 2008722.

CAS | **Web of Science®** | **Google Scholar**

7　Y. Xiao, W. Xiao, D. Wu, L. Guan, M. Luo, L. D. Sun, *Adv. Funct. Mater.* 2022, **32**, 2109618.

CAS | **Web of Science®** | **Google Scholar**

8　L. Li, T. Li, Y. Hu, C. Cai, Y. Li, X. Zhang, B. Liang, Y. Yang, J. Qiu, *Light: Sci. Appl.* 2022, **11**, 51.

CAS | **PubMed** | **Web of Science®** | **Google Scholar**

9　M. Sadraeian, L. Zhang, F. Aavani, E. Biazar, D. Jin, *eLight* 2022, **2**, 18.

PubMed | **Google Scholar**

10　G. Huang, Y. Liu, D. Wang, Y. Zhu, S. Wen, J. Ruan, D. Jin, *eLight* 2022, **2**, 20.

Google Scholar

11　M.-H. Fang, Z. Bao, W.-T. Huang, R.-S. Liu, *Chem. Rev.* 2022, **122**, 11474.

| **CAS** | **PubMed** | **Web of Science®** | **Google Scholar** |

12   X. Feng, L. Lin, R. Duan, J. Qiu, S. Zhou, *Prog. Mater. Sci.* 2022, **129**, 100973.

| **CAS** | **Web of Science®** | **Google Scholar** |

13   Z. Tang, F. Du, H. Liu, Z. Leng, X. Sun, H. Xie, M. Que, Y. Wang, *Adv. Opt. Mater.* 2022, **10**, 2102204.

| **CAS** | **Web of Science®** | **Google Scholar** |

14   J. J. Joos, D. V. der Heggen, L. I. D. J. Martin, L. Amidani, P. F. Smet, Z. Barandiaran, L. Seijo, *Nat. Commun.* 2020, **11**, 3647.

| **CAS** | **PubMed** | **Web of Science®** | **Google Scholar** |

15   S. Jin, R. Li, H. Huang, N. Jiang, J. Lin, S. Wang, Y. Zheng, X. Chen, D. Chen, *Light: Sci. Appl.* 2022, **11**, 52.

| **CAS** | **PubMed** | **Web of Science®** | **Google Scholar** |

16   D. Liu, G. Li, P. Dang, Q. Zhang, Y. Wei, L. Qiu, M. S. Molokeev, H. Lian, M. Shang, J. Lin, *Light: Sci. Appl.* 2022, **11**, 112.

| **CAS** | **PubMed** | **Web of Science®** | **Google Scholar** |

17   S. Wang, R. Pang, T. Tan, H. Wu, Q. Wang, C. Li, S. Zhang, T. Tan, H. You, H. Zhang, *Adv. Mater.* 2023, 2300124.

| **Google Scholar** |

18   Z. Zhou, F. He, E. Song, S. Zhang, X. Yi, H. Zhang, Y. Le, S. Ye, S. Xu, J. Qiu, G. Dong, *Adv. Opt. Mater.* 2023, **11**, 2202466.

| **CAS** | **Web of Science®** | **Google Scholar** |

19   F. Zhao, Z. Song, Q. Liu, *Laser Photon. Rev.* 2022, **16**, 2200380.

| **CAS** | **Web of Science®** | **Google Scholar** |

20   D. Huang, H. Zhu, Z. Deng, H. Yang, J. Hu, S. Liang, D. Chen, E. Maab, W. Guo, *J. Mater. Chem. C* 2021, **9**, 164.

| **CAS** | **Web of Science®** | **Google Scholar** |

21   Y. Zhang, S. Miao, Y. Liang, C. Liang, D. Chen, X. Shan, K. Sun, X.-J. Wang, *Light: Sci. Appl.* 2022, **11**, 136.

| **CAS** | **PubMed** | **Web of Science®** | **Google Scholar** |

22   C. Yuan, R. Li, Y. Liu, L. Zhang, J. Zhang, G. Leniec, P. Sun, Z. Liu, Z. Luo, R. Dong, J. Jiang, *Laser Photon. Rev.* 2021, **11**, 2100227.

| **Google Scholar** |

23   F. He, E. Song, Y. Zhou, H. Ming, Z. Chen, J. Wu, P. Shao, X. Yang, Z. Xia, Q. Zhang, *Adv. Funct. Mater.* 2021, **31**, 2103743.

| **CAS** | **Web of Science®** | **Google Scholar** |

24   Z. Jia, C. Yuan, Y. Liu, X.-J. Wang, P. Sun, L. Wang, H. Jiang, J. Jiang, *Light: Sci. Appl.* 2020, **9**, 86.

| **CAS** | **PubMed** | **Web of Science®** | **Google Scholar** |

25   E. T. Basore, W. Xiao, X. Liu, J. Wu, J. Qiu, *Adv. Opt. Mater.* 2020, **8**, 2000296.

| **CAS** | **Web of Science®** | **Google Scholar** |

26   G. Zheng, W. Xiao, H. Wu, J. Wu, X. Liu, J. Qiu, *Laser Photon. Rev.* 2021, **15**, 2100060.

| **CAS** | **Web of Science®** | **Google Scholar** |

27   R. Li, Y. Liu, C. Yuan, G. Leniec, L. Miao, P. Sun, Z. Liu, Z. Luo, R. Dong, J. Jiang, *Adv. Opt. Mater.* 2021, **9**, 2100388.

| **CAS** | **Web of Science®** | **Google Scholar** |

28   H. Xiao, J. Zhang, L. Zhang, H. Wu, H. Wu, G. Pan, F. Liu, J. Zhang, *Adv. Opt. Mater.* 2021, **20**, 2101134.

| **Google Scholar** |

29   B. Malysa, A. Meijerink, T. Jüstel, *J. Lumin.* 2021, **202**, 523.

| **Google Scholar** |

30 M. Mao, T. Zhou, H. Zeng, L. Wang, F. Huang, X. Tang, R.-J. Xie, *J. Mater. Chem. C* 2020, **8**, 1981.

CAS | **Web of Science®** | **Google Scholar**

31 Y. Jin, Z. Zhou, R. Ran, S. Tan, Y. Liu, J. Zheng, G. Xiang, L. Ma, X.-J. Wang, *Adv. Opt. Mater.* 2022, **10**, 2202049.

CAS | **Web of Science®** | **Google Scholar**

32 H. Jiang, L. Chen, G. Zheng, Z. Luo, X. Wu, Z. Liu, R. Li, Y. Liu, P. Sun, J. Jiang, *Adv. Opt. Mater.* 2022, **10**, 2102741.

CAS | **Web of Science®** | **Google Scholar**

33 B. Struve, G. Huber, V. V. Laptev, I. A. Shcherbakov, E. V. Zharikov, *Appl. Phys. B* 1983, **30**, 117.

Web of Science® | **Google Scholar**

34 B. Struve, G. Huber, *Appl. Phys.* 1985, **36**, 195.

Web of Science® | **Google Scholar**

35 K. Elzbieciak, A. Bednarkiewicz, L. Marciniak, *Sensor. Actuat. B-Chem.* 2018, **269**, 96.

CAS | **Web of Science®** | **Google Scholar**

36 A. Zabiliūtė, S. Butkutė, A. Žukauskas, P. Vitta, A. Kareiva, *Appl. Opt.* 2014, **53**, 907.

CAS | **PubMed** | **Web of Science®** | **Google Scholar**

37 X. Zou, X. Wang, H. Zhang, Y. Kang, X. Yang, X. Zhang, M. S. Molokeev, B. Lei, *Chem. Eng. J.* 2022, **428**, 132003.

CAS | **Web of Science®** | **Google Scholar**

38 Y. Wang, Z. Wang, G. Wei, Y. Yang, S. He, J. Li, Y. Shi, R. Li, J. Zhang, P. Li, *Adv. Opt. Mater.* 2022, **10**, 2200415.

CAS | **Web of Science®** | **Google Scholar**

39 Y. Wang, Z. Wang, G. Wei, Y. Yang, S. He, J. Li, Y. Shi, R. Li, J. Zhang, P. Li, *Chem. Eng. J.* 2022, **437**, 135346.

| **CAS** | **Web of Science®** | **Google Scholar** |

40 R. D. Shannon, *Acta Cryst* 1976, **32**, 751.

| **CAS** | **Google Scholar** |

41 Y. Tanabe, S. Sugano, *J. Phys. Soc. Jpn.* 1954, **9**, 766.

| **CAS** | **Web of Science®** | **Google Scholar** |

42 B. Michele, U. Jumpei, M. G. Brik, T. Setsuhisa, *ACS Appl. Mater. Interfaces* 2020, **12**, 38325.

| **PubMed** | **Web of Science®** | **Google Scholar** |

43 Y. Liu, J. Silver, R.-J. Xie, J. Zhang, H. Xu, H. Shao, J. Jiang, *J. Mater. Chem. C* 2017, **5**, 12365.

| **CAS** | **Web of Science®** | **Google Scholar** |

44 D. Wen, H. Liu, Y. Guo, Q. Zeng, M. Wu, R.-S. Liu, *Angew. Chem., Int. Ed.* 2022, **61**, e202204411.

| **CAS** | **PubMed** | **Web of Science®** | **Google Scholar** |

45 K. Zhao, X. Xu, W. Ren, P. Xi, *eLight* 2022, **2**, 5.

| **CAS** | **Google Scholar** |

46 P. Qi, Y. Luo, B. Shi, W. Li, D. Liu, L. Zheng, Z. Liu, Y. Hou, Z. Fang, *eLight* 2021, **1**, 6.

| **Google Scholar** |

47 X. Xu, Q. Shao, L. Yao, Y. Dong, J. Jiang, *Chem. Eng. J.* 2020, **383**, 123108.

| **CAS** | **Web of Science®** | **Google Scholar** |

48 J. Qiao, S. Zhang, X. Zhou, W. Chen, R. Gautier, Z. Xia, *Adv. Mater.* 2022, **34**, 2201887.

| **CAS** | **Web of Science®** | **Google Scholar** |

49 G. Wei, Z. Wang, R. Li, Y. Wang, J. Li, Y. Shi, S. He, Y. Yang, Z. Yang, P. Li, *Adv. Opt. Mater.* 2022, **10**, 2201076.

| **CAS** | **Web of Science®** | **Google Scholar** |

50 R. Li, P. Li, G. Wei, J. Li, Y. Shi, Y. Wang, S. He, Y. Yang, W. Ding, Z. Wang, *Ceram. Int.* 2023, **49**, 6246.

| **CAS** | **Web of Science®** | **Google Scholar** |

Citing Literature

Download PDF

ABOUT WILEY ONLINE LIBRARY

Privacy Policy
Terms of Use
About Cookies
Manage Cookies
Accessibility
Wiley Research DE&I Statement and Publishing Policies
Developing World Access

HELP & SUPPORT

Contact Us
Training and Support
DMCA & Reporting Piracy

OPPORTUNITIES

Subscription Agents
Advertisers & Corporate Partners

CONNECT WITH WILEY

The Wiley Network
Wiley Press Room